JOURNAL OF GEOPHYSICAL RESEARCH, VOL. 116, A05106, doi:10.1029/2011JA016490, 2011

Energy transfer during intense geomagnetic storms driven by interplanetary coronal mass ejections and their sheath regions

Jianpeng Guo,[1] Xueshang Feng,[1] Barbara A. Emery,[2] Jie Zhang,[3] Changqing Xiang,[1] Fang Shen,[1] and Wenbin Song[1]

Received 21 January 2011; revised 2 March 2011; accepted 18 March 2011; published 28 May 2011.

[1] The interaction of the solar wind and Earth's magnetosphere is complex, and the phenomenology of the interaction is very different for interplanetary coronal mass ejections (ICMEs) compared to their sheath regions. In this paper, a total of 71 intense ($Dst \leq -100$ nT) geomagnetic storm events in 1996–2006, of which 51 are driven by ICMEs and 20 by sheath regions, are examined to demonstrate similarities and differences in the energy transfer. Using superposed epoch analysis, the evolution of solar wind energy input and dissipation is investigated. The solar wind-magnetosphere coupling functions and geomagnetic indices show a more gradual increase and recovery during the ICME-driven storms than they do during the sheath-driven storms. However, the sheath-driven storms have larger peak values. In general, solar wind energy input (the epsilon parameter) and dissipation show similar trends as the coupling functions. The trends of ion precipitation and the ratio of ion precipitation to the total (ion and electron) are quite different for both classes of events. There are more precipitating ions during the peak of sheath-driven storms. However, a quantitative assessment of the relative importance of the different energy dissipation branches shows that the means of input energy and auroral precipitation are significantly different for both classes of events, whereas Joule heating, ring current, and total output energy display no distinguishable differences. The means of electron precipitation are significantly different for both classes of events. However, ion precipitation exhibits no distinguishable differences. The energy efficiency bears no distinguishable difference between these two classes of events. Ionospheric processes account for the vast majority of the energy, with the ring current only being 12%–14% of the total. Moreover, the energy partitioning for both classes of events is similar.

Citation: Guo, J., X. Feng, B. A. Emery, J. Zhang, C. Xiang, F. Shen, and W. Song (2011), Energy transfer during intense geomagnetic storms driven by interplanetary coronal mass ejections and their sheath regions, *J. Geophys. Res.*, *116*, A05106, doi:10.1029/2011JA016490.

1. Introduction

[2] Manifestations of coronal mass ejections (CMEs) from the Sun are frequently observed in the solar wind near Earth and are commonly called interplanetary coronal mass ejections (ICMEs). ICMEs are also called ejecta, which could be either magnetic clouds (MCs) or noncloud ejecta. ICMEs moving faster than the ambient solar wind will compress and deflect the upstream flow. If the relative speed of the two plasma regimes is greater than the fast mode MHD wave speed, then a fast shock will form ahead of the ICME. The region of the compressed solar wind bounded by the shock front and the ICME's leading edge is referred to as the sheath region. Within a sheath the direction of the magnetic field can change several times from south to north while within an ICME the magnetic field direction typically changes smoothly over timescales of a day. The passage of southward directed (Bs) interplanetary magnetic field (IMF) in both ICME and sheath can drive strong magnetospheric activity [e.g., *Gonzalez and Tsurutani*, 1987; *Tsurutani et al.*, 1988; *Gonzalez et al.*, 1994; *Richardson et al.*, 2002; *Huttunen and Koskinen*, 2004; *Zhang et al.*, 2007, 2008b]. *Guo et al.* [2010a] compared the geoefficiency of ICMEs and sheath regions in the near-Earth space by using solar wind-magnetosphere coupling functions, and found that these two structures show comparable Newell function [*Newell et al.*, 2007], whereas they reveal statistically

[1]SIGMA Weather Group, State Key Laboratory of Space Weather, CSSAR, Chinese Academy of Sciences, Beijing, China.
[2]High Altitude Observatory, NCAR, Boulder, Colorado, USA.
[3]Department of Computational and Data Sciences, George Mason University, Fairfax, Virginia, USA.

0148-0227/11/2011JA016490

meaningful differences in the dayside reconnection rate according to the Borovsky function [*Borovsky*, 2008]. Furthermore, the passages of sheath regions are usually short in duration, because their radial sizes are smaller than that of corresponding ICMEs [e.g., *Forsyth et al.*, 2006; *Lepping et al.*, 2006; *Gopalswamy*, 2006; *Yermolaev et al.*, 2007, 2009; *Gopalswamy et al.*, 2008; *Zhang et al.*, 2008a]. Therefore, it is interesting to separate magnetospheric activity due to ICME and the compressed sheath region that precedes ICMEs since the solar wind parameters that control solar wind-magnetospheric coupling have a significantly different behavior within these structures. In fact, significant differences in the magnetospheric response between ICMEs and their preceding sheath regions have been reported [e.g., *Huttunen et al.*, 2002, 2006, 2008; *Huttunen and Koskinen*, 2004; *Koskinen and Huttunen*, 2006; *Pulkkinen et al.*, 2007]. For instance, the storms driven by sheath regions have stronger auroral activity, stronger magnetotail field stretching, larger asymmetry in the inner magnetosphere field configuration, and larger asymmetric ring current, while the ring current enhancement is stronger in the storms driven by magnetic clouds [*Huttunen et al.*, 2002, 2006; *Pulkkinen et al.*, 2007].

[3] Geomagnetic storms represent a significant dissipation of energy through the magnetosphere. The energy that is derived from the solar wind flow and the subsequent powerful conversion of that energy takes several different forms. Ring current injection and decay, ionospheric Joule heating, particle precipitation into the atmosphere, and several related physical processes are noticed clearly in large storm events [e.g., *Akasofu*, 1981; *Knipp et al.*, 1998; *Lu et al.*, 1998; *Baker et al.*, 2001; *Koskinen and Tanskanen*, 2002; *Pulkkinen et al.*, 2002; *Tanskanen et al.*, 2002; *Feldstein et al.*, 2003; *Palmroth et al.*, 2003; *Vichare et al.*, 2005; *Guo et al.*, 2008, 2010b; *Turner et al.*, 2009]. It is particularly important to determine how much energy is absorbed by the magnetosphere from the solar wind flow during storm events. Given such a determination, it is of further great value to understand quantitatively how this input energy is partitioned among the various "branches" that represent the energy dissipation occurring during storms. Moreover, previous research works found that the ratio of measured energy output to estimated energy input (the geoefficiency) varied with the type of the solar wind driver [*Turner et al.*, 2006, 2009; *Lu*, 2006].

[4] *Richardson et al.* [2002] separated solar wind structures into transient solar wind structures, high-speed streams (HSS), and slow speed wind. The transient solar wind structures are ICMEs and their preceding associated shocks and compressed sheath regions. These transient structures maximize during solar maximum, and account for the largest minimum *Dst* in magnetic storms. HSS are usually preceded by compressed corotating interaction regions (CIRs) and are prominent in the descending and minimum phases of the solar cycle. *Turner et al.* [2006, 2009] compared the geoefficiency and the energy partitioning of magnetic storms related to ICMEs with those related to the longer-lasting CIRs with HSS. They found that the average energy output of CME storms to be larger than CIR storms, but the geoefficiency of CIR storms to be greater than CME storms. They did not differentiate the ICME storms from those driven by their sheath regions, as we propose to do in the present study.

[5] These factors motivate the present study: to investigate similarities and differences in energy input and dissipation during the ICME- and sheath-driven storms. Note, in this paper, geomagnetic storms driven by ICMEs and their preceding sheath regions are termed as ICME-driven storms and sheath-driven storms, respectively. The statistical studies by *Zhang et al.* [2007] and *Guo et al.* [2010a] suggest that these two structures have comparable energy transfer efficiencies. Thus, the relative contribution is mainly caused by the amount of the time spent within each of the structures, and the ICME usually dominates energy input into the magnetosphere during these storms. The differences in energy input and dissipation during the ICME- and sheath-driven storms could be possibly responsible for the differences in the magnetospheric responses noted above.

2. Event Selection and Analysis Methods

[6] The storm events are selected from the list of the 90 intense geomagnetic storms ($Dst \leq -100$ nT) complied by *Zhang et al.* [2007, 2008b]. This list covers the period from 1996 to 2006. When considering only the main dip associated with the peaks of each intense storm, they found that 51 of these 90 main dips were caused by ICMEs, 20 by sheath regions, 9 by shocks propagating through preceding ICMEs, and 10 by corotating interaction regions. In this study, we focus our efforts on two sets of drivers: (1) ICMEs and (2) the sheath regions preceding ICMEs. Thus, we select a total of 71 storms, of which 51 are mainly driven by ICMEs and 20 by sheath regions. As an ICME is often preceded by a sheath region, an ICME-driven storm may be affected by both the ICME structure and the preceding sheath. However, this kind of contamination by the sheath may not be significant, since the mean IMF Bs in ICMEs are much larger than those in the sheath regions for most ICME-driven events [e.g., *Zhang et al.*, 2007, 2008a]. Moreover, the radial sizes of the ICMEs are also much larger. Similarly, a sheath-driven storm may also be affected by the ICME structure. The contamination by the ICME may also not be significant for our results, since for the selected sheath-driven events, the IMF turns rapidly northward at the peak of the storm and remains northward in the recovery for the sheath-driven storms (shown in Figure 1). In any case, the "contamination" of ICME and sheath tends to dilute the distinct geoeffective effects between the two types of drivers. For each storm, the solar wind magnetic field and plasma parameters are available from the 1 h averaged OMNI database (GSM coordinates at 1 AU).

[7] For these ICMEs and sheath events, superposed epoch analyses are carried out on solar wind parameters, wind-magnetosphere coupling functions, geomagnetic indices, and solar wind energy input and dissipation data, in order to show similarities and differences in the temporal evolution of energy transfer during the ICME- and sheath-driven storms. For cloud-driven storms, a standard "trigger" to take for the zero epoch of the data superposition is the minimum value of the *Dst* index for the storm. Taking a single trigger at *Dst* minimum to analyze CME-driven storms is a method that mixes several cloud-driven storm phases together

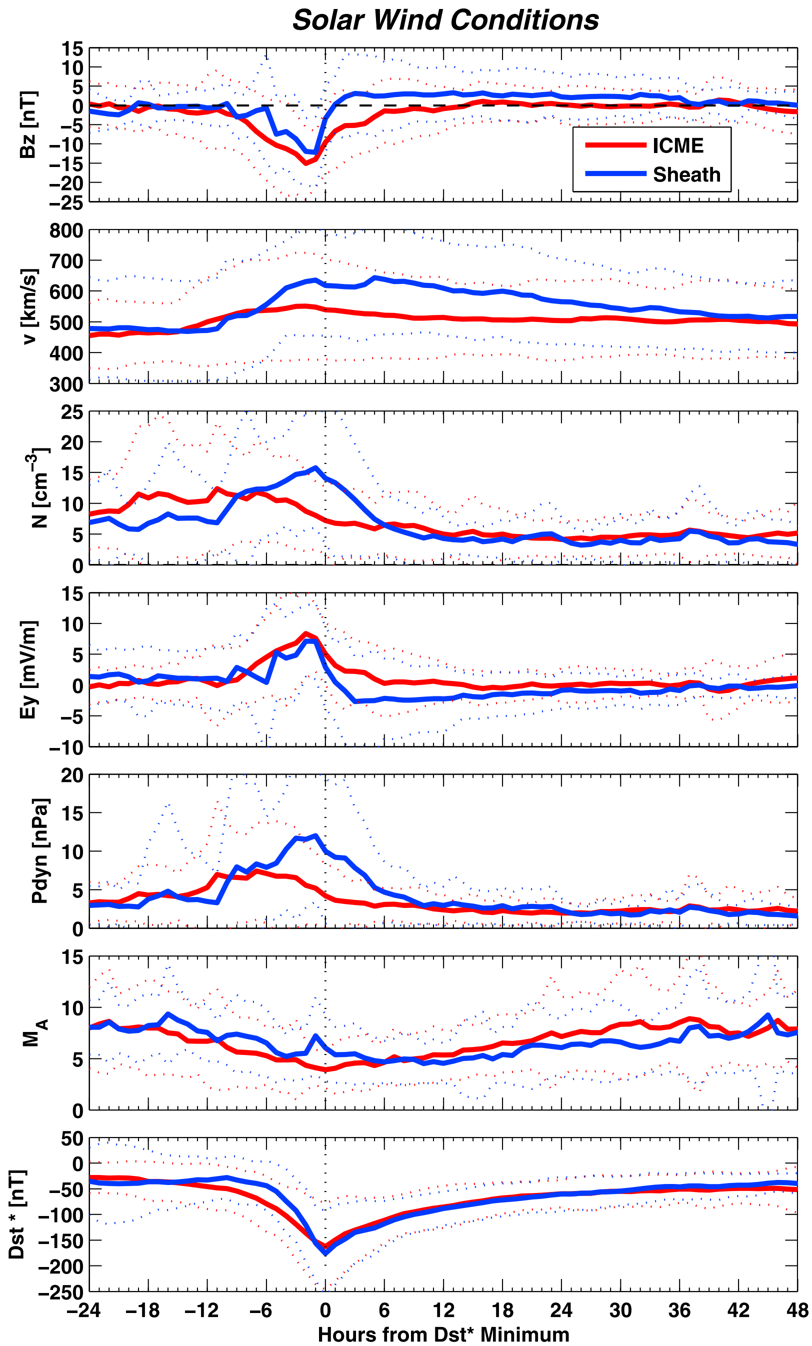

Figure 1. Superposed solar wind parameters during the ICME- and sheath-driven storms. Epoch time is set to be the minimum value of the *Dst** index for each storm, indicated by the vertical dashed line. From top to bottom: the IMF Bz, the solar wind speed v, the solar wind density N, the Y component of the electric field Ey, the dynamic pressure Pdyn, the Alfvén Mach number M_A, and the *Dst** index. The red and blue solid lines define the mean for the ICME- and sheath-driven storms, respectively, and the dotted lines represent ±1 standard deviation.

owing to the storm-to-storm differences in the sequences, and to the different temporal durations of the phases. Similarly, in the present study the zero epoch time used is the trigger on the minimum value of *Dst**. The *Dst** index is the solar wind dynamic pressure-corrected *Dst* index. According to the paper of *Burton et al.* [1975], $Dst^* = Dst - bP^{1/2} + c$, where P is the solar wind dynamic pressure and the constants b and c are b = 7.26 and c = 11.0 as derived by *O'Brien and McPherron* [2000]. Data are taken from 24 h prior to and 48 h following the zero epoch to cover the period from storm onset through to recovery.

[8] In addition to the temporal evolution of energy transfer, for each storm, we also estimate the integrated values of the energy input and the energy dissipated via ring current, Joule heating and auroral precipitation, which we have summed and referred to as energy output. Each storm

is considered to begin at the first decrease in *Dst** and end when the *Dst** has recovered 80% from its lowest value. In what follows we examine statistically similarities and differences in energy partitioning for the ICME- and sheath-driven storms.

3. Superposed Epoch View

3.1. Solar Wind Behavior

[9] Figure 1 shows the superposed epoch analysis for selected solar wind parameters for the ICME- and sheath-driven storms. From top to bottom are the IMF B_Z, the solar wind speed v, the solar wind density N, the Y component of the electric field Ey, the dynamic pressure Pdyn, the Alfvén Mach number M_A and the *Dst** index. The red and blue solid lines define the mean for the ICME- and sheath-driven storms, respectively, and the dotted lines represent ±1 standard deviation. The trigger time marked by the vertical dashed line is the zero epoch, the minimum value of the *Dst** index. Typical signatures of solar wind structures can be seen in the trends in the solar wind data used in the superposed epoch study. The time profile of IMF Bz shows a more gradual change and its peak is slightly greater during the ICME-driven storms than it is during the sheath-driven storms. On average, the solar wind velocity and dynamic pressure are considerably higher for the sheath-driven storms compared to the ICME-driven storms. The solar wind density for the ICME-driven storms is larger than that for the sheath-driven storms within the period from −24 h to −9 h of the epoch, and then the opposite situation occurs within the period from −9 h to 6 h of the epoch. Later, the density is comparable for both classes of events. During the storm main phase, the electric field Ey for the sheath-driven storms and the ICME-driven storms are comparable. However, Ey turns dawnward and remains dawnward during the recovery phase for the sheath-driven storms compared to the ICME-driven storms. The Alfvén Mach number in the early phase (from −18 h to 8 h of the epoch) is larger for the sheath-driven storms compared to the ICME-driven storms, and the opposite is true in the later phase.

3.2. Coupling Efficiency of the Solar Wind With the Magnetosphere

[10] To investigate the coupling efficiency of the solar wind with the magnetosphere during the ICME- and sheath-driven storms, we use two types of solar wind-magnetosphere coupling functions, namely, the solar wind "driver function" and the solar wind "control function" (cf. *Borovsky*, 2008). The driver functions are derived with "tuning" to optimize correlation coefficients between magnetospheric measurements and solar wind measurements, while there are no explicit free parameters in the control function.

[11] The solar wind driver function used is the Newell formula (equation (1)) [*Newell et al.*, 2007]:

$$d\Phi/dt = v^{4/3} B_T^{2/3} \sin^{8/3}\left(\frac{\theta}{2}\right) \quad (1)$$

The variables v, B_T, and θ on the right-hand side are given in SI units and denote the solar wind velocity, the solar wind magnetic field perpendicular to the Sun-Earth line, and the IMF clock angle, respectively. The Newell formula was found to be better correlated with the magnetic indices than other candidate coupling functions listed in the work of *Newell et al.* [2007, Table 1]. That is the reason why the Newell formula is selected for this study.

[12] The solar wind control function used is the Borovsky function [*Borovsky*, 2008]; that is, a reconnection rate written in terms of upstream solar wind parameters:

$$R = 0.4\mu_0^{1/2} \sin(\theta/2)\rho v^2 \left(1 + 0.5M_{ms}^{-2}\right)(1+\beta_s)^{-1/2} \cdot \left[C\rho + (1+\beta_s)^{-1/2}\rho_m\right]^{-1/2} \left[(1+\beta_s)^{1/2} + 1\right]^{-1/2} \quad (2)$$

where β_s

$$\beta_s = 3.2 \times 10^{-2} M_A^{1.92} \quad (3)$$

is the plasma beta of the magnetosheath near the nose of the magnetosphere,

$$C = \{[1/4]^6 + [1/(1 + 1.38\log_e(M_A))]^6\}^{-1/6} \quad (4)$$

is the compression ratio of the bow shock,

$$M_{ms} = v/((B/4\pi\rho) + 2P/\rho)^{1/2} \quad (5)$$

is the magnetosonic Mach number of the solar wind, and

$$M_A = v(4\pi\rho)^{1/2}/B \quad (6)$$

is the Alfvén Mach number of the solar wind. A term $\sin(\theta/2)$ is also added to account for the component reconnection when the IMF has a clock angle of θ. In these expressions v, ρ, B, and P are the speed, mass density, magnetic field strength, and particle pressure (thermal plus kinetic) in the upstream solar wind. In calculating the Borovsky function, we take $\rho_m = 0$ since there is no information available about the dayside magnetospheric mass density ρ_m [see *Guo et al.*, 2010a]. The control function was found to be successful, as good as the best solar wind driver function in the literature [*Borovsky*, 2008].

[13] Figure 2 shows the results of superposed epoch analyses for the Newell parameter and the Borovsky parameter during the ICME- and sheath-driven storms. The Newell parameter shows a more gradual increase and recovery during the ICME-driven storms than it does during the sheath-driven storms. The peak values occur at about 1 to 2 h prior to the zero epoch, moreover, it is slightly larger for the sheath-driven storms. On average, the Newell parameter is larger for the ICME-driven storms. The Borovsky parameter trends in a similar way to the Newell parameter.

3.3. Geomagnetic Response

[14] The geomagnetic activity is examined using seven indices: *AL*, *AU*, *PC*, *Kp*, *SYM-H*, *ASYH*, and *Dst**. *AL* and *AU* are the auroral electrojet indices, where the total electroject *AE* = *AU*–*AL*. The *PC* index derived from polar magnetic variations is primarily a measure of the intensity of the transpolar ionospheric currents generated by the solar wind interaction with Earth's magnetosphere. We use the northern hemisphere *PCN* index from Thule in this study. The *Kp* index can be used to categorize storm intensity and

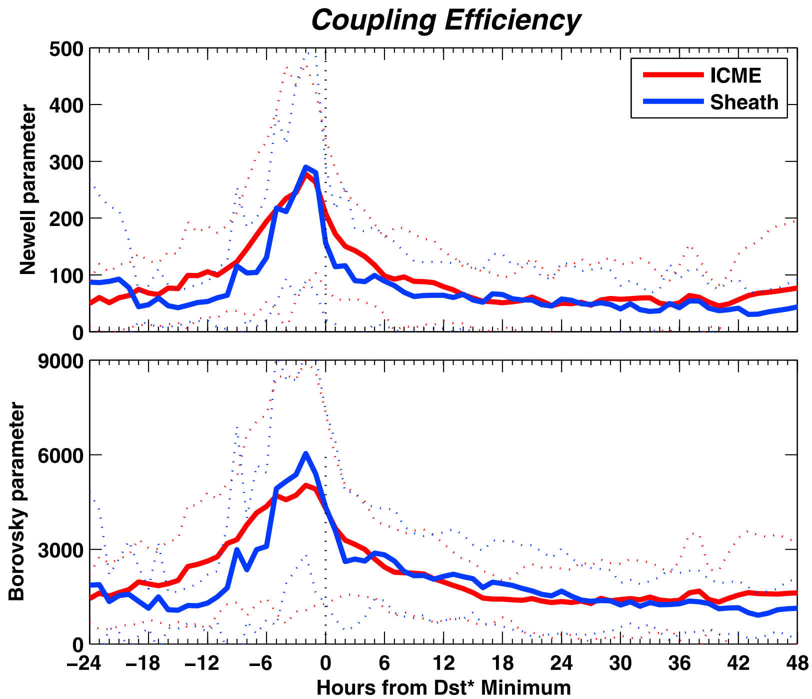

Figure 2. Superposed solar wind driver function (Newell parameter) and solar wind control function (Borovsky parameter) during the ICME- and sheath-driven storms. The red and blue solid lines define the mean for the ICME- and sheath-driven storms, respectively, and the dotted lines represent ±1 standard deviation.

is a proxy for the strength of magnetospheric convection [e.g., *Thomsen*, 2004]. The *SYM-H* index is a similar measure to the *Dst* index but has a 1 min resolution. The higher resolution means that the *SYM-H* index can be used to investigate geomagnetic activity on a smaller temporal scale, such as sudden impulses (SI). The *ASYH* index is a measure of the degree of asymmetry in the midlatitude magnetic records, given as a maximum difference between measurements at different longitudes. The *Dst** index is the solar wind dynamic pressure-corrected *Dst* index (described above), which is considered to be a measure of intensity of the ring current and can be used to categorize storm intensity.

[15] Figure 3 shows the superposed geomagnetic indices during the ICME- and sheath-driven storms. The auroral and polar cap activity shows a faster increase and recovery for the sheath-driven storms. The peak value of *Kp* is slightly greater for the sheath-driven storms, but the average *Kp* remains elevated over a longer period of time during the ICME-driven storms especially before the *Dst** minimum, implying a longer period of the magnetospheric convection. The *ASYH* index is significantly larger around the time of the zero epoch for the sheath-driven storms. The maximum values of the *SYM-H* indices for both sets are almost equal. Furthermore, as we can see from the profiles of *Dst** (cf. Figure 1), the sheath-driven storms show a faster response at storm onset defined as the time when *Dst** starts to decrease and shorter duration of the main phase defined as the time interval from onset to *Dst** minimum: The main phase averages are 8 h for the sheath-driven storms and 14 h for the ICME-driven storms. This is consistent with the result of *Pulkkinen et al.* [2007]. The intensity at storm maximum is slightly larger for the sheath-driven storms (Dst* = −176 nT) compared to the ICME-driven storms (Dst* = −163 nT). However, this difference is not statistically significant. The recoveries defined as the time after *Dst** minimum for both classes of events are quite similar.

3.4. Solar Wind Energy Input and Dissipation

[16] At present, there are no direct observational means of determining the energy transfer from the solar wind to the magnetosphere and thermosphere-ionosphere system. In fact, we do not even know the details of how and where the transfer takes place. The need to have useful estimates of energy available for magnetospheric dynamics has led to the formulation of a large number of coupling functions [*Koskinen and Tanskanen*, 2002]. For the present study, we use the well-known Akasofu function (or the epsilon parameter) (equation (7)) [*Akasofu*, 1981]:

$$\varepsilon(W) = \frac{4\pi}{\mu_0} vB^2 \sin^4\left(\frac{\theta}{2}\right) l_0^2 \qquad (7)$$

The variables v, B, θ, and l_0 on the right-hand side are given in SI units and denote the solar wind velocity, the solar wind magnetic field magnitude, the IMF clock angle, and the scaling factor, respectively. The scaling factor was empirically determined to be l_0 = 7 R_E [*Perreault and Akasofu*, 1978]. It is scaled to numerically correspond to the estimated energy output in the magnetosphere and the physical dimension of power for the energy input rate [*Koskinen and Tanskanen*, 2002]. It is important to point out that the

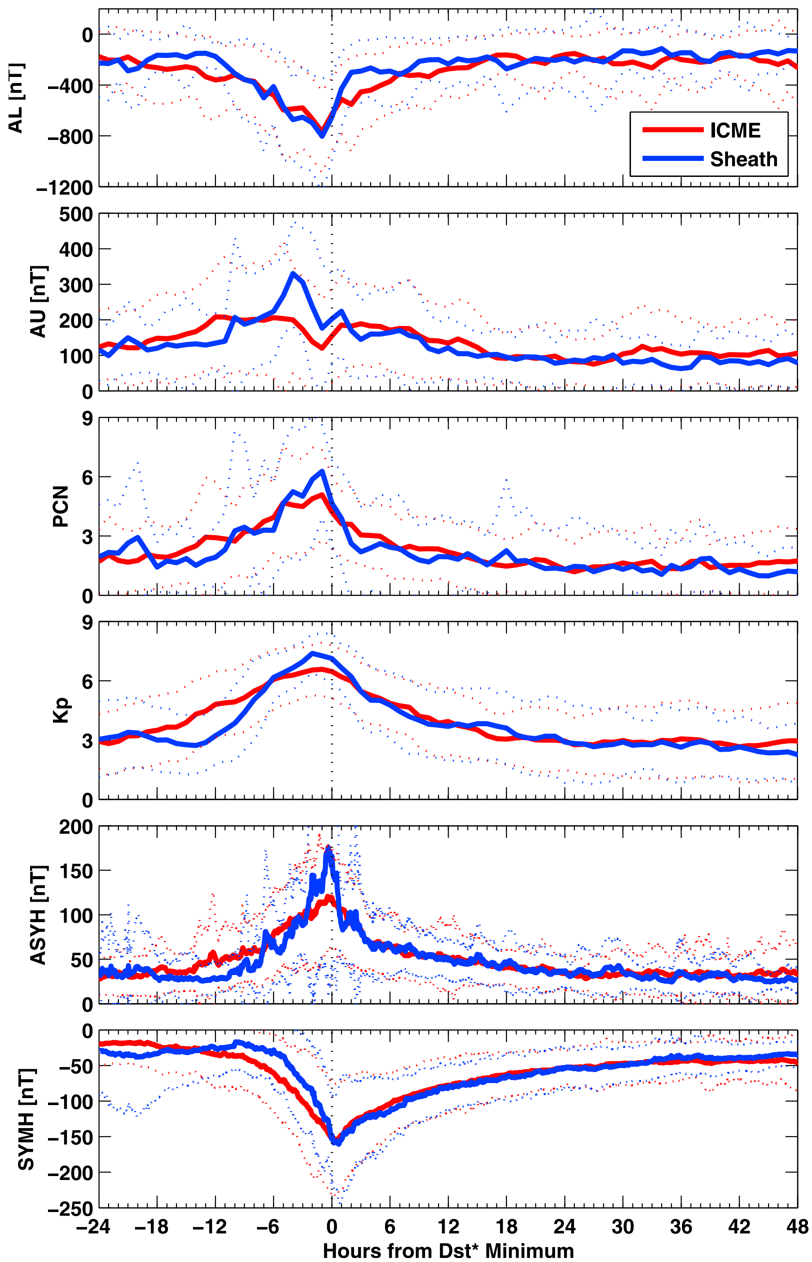

Figure 3. Superposed geomagnetic indices during the ICME- and sheath-driven storms. From top to bottom: *AL*, *AU*, *PCN*, *Kp*, *ASYH*, and *SYM-H*. The red and blue solid lines define the mean for the ICME- and sheath-driven storms, respectively, and the dotted lines represent ±1 standard deviation.

epsilon parameter allows some knowledge of when more energy is available and scales well with the energy output, but does not necessarily capture the correct magnitude of solar wind energy input [cf. *Turner et al.*, 2009].

[17] Figure 4 shows the superposed solar wind energy input using the epsilon parameter during the ICME- and sheath-driven storms. The epsilon parameter trends in a similar way as the Newell parameter and the Borovsky parameter. On average, the epsilon parameter is larger for the ICME-driven storms, but the peak value is slightly larger for the sheath-driven storms.

[18] As noted above, the energy output is the sum of auroral precipitation, Joule heating, and ring current. To estimate the energy output, we use the same methodology as that in the work of *Turner et al.* [2006, 2009], which is briefly described below.

[19] Global auroral precipitation estimates are computed using data from Defense Meteorological Satellite Program (DMSP) and National Oceanic and Atmospheric Administration (NOAA) satellites intercalibrated with each other by *Emery et al.* [2008, 2009]. NOAA satellites provide estimates of the total hemispheric power (HPt) from both electron and ion sensors for energies <20 keV while the DMSP satellites provide estimates of the electron hemispheric power (HPe) from the electron sensors for energies <20 keV ignoring the highest-energy channel between 20.62 keV and 30.18 keV [*Emery et al.*, 2008]. The ion hemispheric power (HPi) is deduced from the NOAA

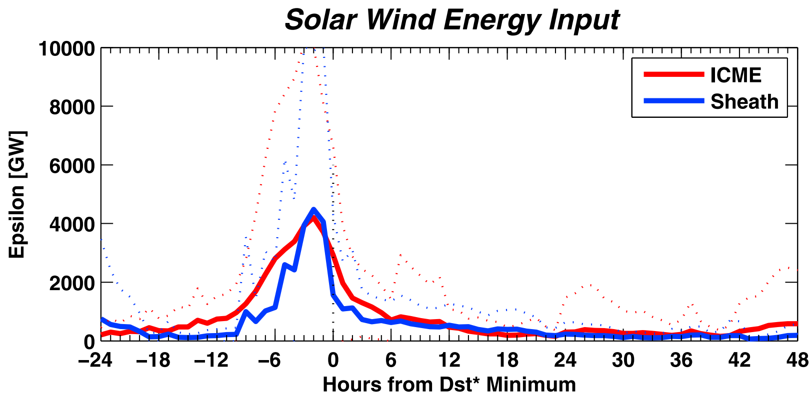

Figure 4. Superposed epoch analyses of solar wind energy input using the epsilon parameter during the ICME- and sheath-driven storms. The red and blue solid lines define the mean for the ICME- and sheath-driven storms, respectively, and the dotted lines represent ±1 standard deviation.

satellites from the difference of the total and the electron hemispheric powers (HPi = HPt-HPe), and account for ~10% of the total HPt [*Emery et al.*, 2008]. The ion fraction of the HPt for <20 keV energies is ~15%, ~7%, and ~8%–10% for *Kp*~0, *Kp*~4 to 6, and *Kp* > 6+, respectively [*Emery et al.*, 2008]. Because the seasonal variations, IMF Bz responses, and solar rotational amplitudes are different between ions and electrons [*Emery et al.*, 2008; B. A. Emery et al., Solar rotation periodicities and the semiannual variation in the solar wind, radiation belt, and aurora, submitted to Solar Physics, 2010], we calculate the global auroral ion (Pi) and electron (Pe) inputs from the sum of the hourly HPi and HPe estimates from each hemisphere for the present study. The high energy contribution (>20 keV) to Pi is estimated to be similar in magnitude to the low-energy component (<20 keV) for *Kp* > 3+ [*Fang et al.*, 2007; *Emery et al.*, 2008], leading to ion percentages of ~20% of the total HPt. In this study, we confine ourselves to auroral energies <20 keV.

[20] Joule heating is estimated using relations derived by *Knipp et al.* [2004]:

$$JH_{summer} = 29.27|PC| + 8.18PC^2 - 0.04|Dst| + 0.0126Dst^2 \quad (8)$$

$$JH_{equinox} = 29.14|PC| + 2.54PC^2 + 0.21|Dst| + 0.0023Dst^2 \quad (9)$$

$$JH_{winter} = 13.36|PC| + 5.08PC^2 + 0.47|Dst| + 0.0011Dst^2 \quad (10)$$

where PC is the *PC* index, Dst is the *Dst* index, summer is defined as 21 April to 20 August, winter is 21 October to 20 February, and equinox is 21 February to 20 April and 21 August to 20 October. For equinox times, northern hemisphere values are doubled to obtain a global value. For summer and winter dates, a Joule heating estimate for summer is added to a winter estimate to account for the hemispheric seasonal differences. The resulting power values are measured in megawatts.

[21] In addition to the energy dissipated into the high-latitude ionosphere through Joule heating and auroral precipitation, energy that has been stored in the magnetosphere is partly converted into ring current energization. We invoke the empirical formula of *Akasofu* [1981] to estimate the ring current energy injection rate:

$$U_{RC} = -4 \times 10^{13}\left(\frac{\partial Dst}{\partial t} + \frac{Dst}{\tau}\right) \quad (11)$$

where τ in seconds is the ring current decay time and set to 8 h in the present study [*Vichare et al.*, 2005]. Before applying this formula (11), corrections should be made to the *Dst* index. First, the *Dst* index is the pressure corrected according to *Burton et al.* [1975] (described above), in order to remove the effects of magnetopause currents, and further 46% of it is subtracted to remove the influence of induced ground currents and tail currents (see *Turner et al.* [2001] for details).

[22] Figure 5 shows the superposed auroral precipitation (Pt = Pi + Pe for <20 keV), Joule heating, ring current and their total output during the ICME- and sheath-driven storms. The auroral precipitation shows a faster increase and recovery for the sheath-driven storms. The profiles of the Joule heating for both classes of events are similar. The profiles of ring current for both classes of events are quite different before the zero epoch, whereas they are almost overlapped after the zero epoch. The trends of total energy output are similar for both classes of events because Joule heating is dominant.

[23] In addition, it is interesting to further investigate whether there are differences in the global auroral electron (Pe) and ion (Pi) inputs between these two classes of storms. Figure 6 shows the superposed Pe and Pi as well as the ratio of Pi to the total (Pt = Pe + Pi) during these two classes of storms. The profile of Pe shows a faster increase and recovery for the sheath-driven storms. However, the peak values of Pe are comparable for both classes of events. The profile of Pi shows a faster increase and recovery for the sheath-driven storms, where the peak value of Pi is significantly larger for the sheath-driven storms. The ratio of Pi to the total Pt is significantly enhanced around 6 h prior to the zero epoch for the sheath-driven storms when Bz exceeds −5 nT and the solar wind speed v exceeds 500 km/s in Figure 1. Usually for Bz increasing negative and v <525 km/s, electron precipitation increases more rapidly than ion precipitation, so there is a decline in Pi/Pt for the ICME-driven

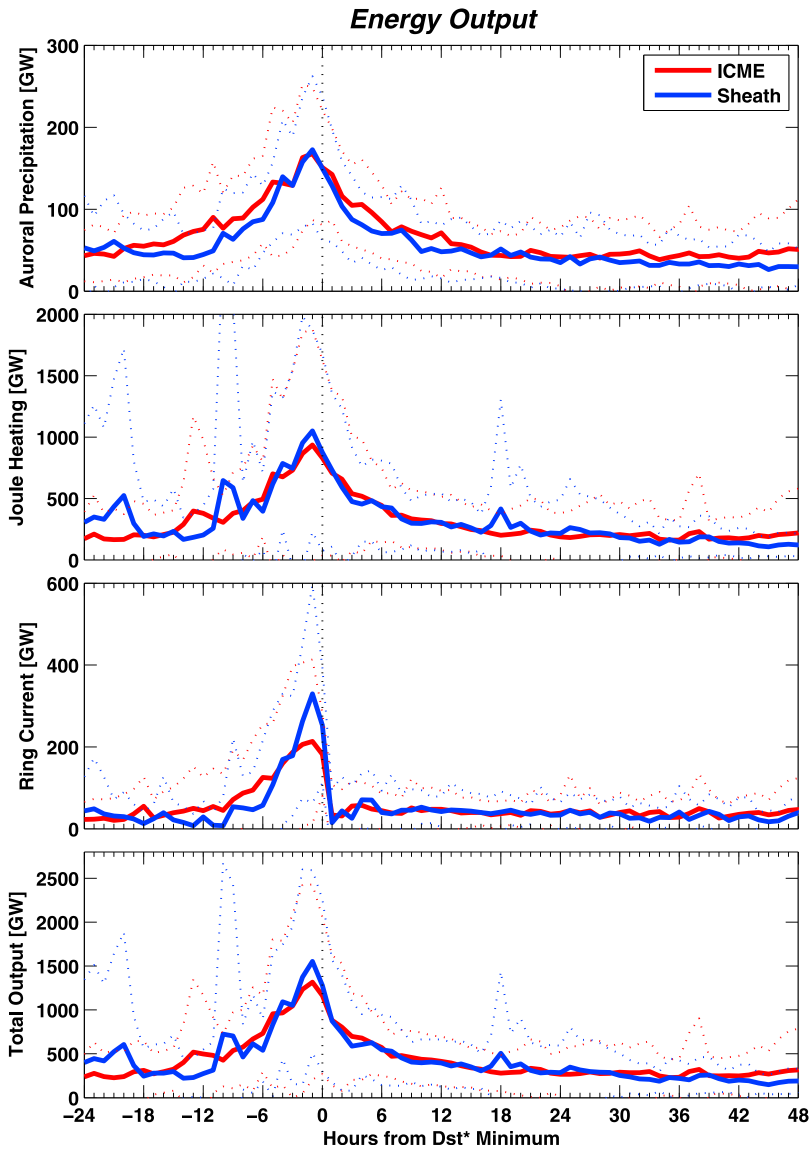

Figure 5. Superposed epoch analyses of energy deposited (auroral precipitation, Joule heating, ring current, and total output) during the ICME- and sheath-driven storms. The red and blue solid lines define the mean for the ICME- and sheath-driven storms, respectively, and the dotted lines represent ±1 standard deviation.

storms before the minimum Bz negative value about 2 h prior to the zero epoch, and a gradual increase in Pi/Pt afterward. For large v and Bz < -5 nT, as well as for all Bz positive conditions, ion precipitation is favored, so the ratio of Pi/Pt for the sheath-driven storms is larger than that for the ICME-driven storms, especially in the Bz positive conditions 1 h after zero epoch [see *Emery et al.*, 2008, Figure 10]. Similarly, 24 h before zero epoch when there appears to be a slow decline in Bz from positive conditions for the ICME-driven storms, the ratio of Pi/Pt is larger for ICME-driven storms than for the sheath-driven storms because ion precipitation is relatively large for Bz positive conditions.

4. Energy Budget and Efficiency for Entire Storm

[24] Although superposed epoch analyses can reveal similarities and differences in the temporal evolution of energy transfer during the ICME- and sheath-driven storms, it is useful to find out whether the differences are statistically meaningful. However, a quantitative assessment of the relative importance of the different energy dissipation branches can provide deeper insight into geomagnetic storms. Therefore, we compute the integrated values of the energy input and dissipation beginning at the first decrease in *Dst** to when the *Dst** has recovered 80% from its lowest value for each storm in both classes of events. The means are listed in Table 1. The energy efficiency of each storm is calculated by equation (12):

$$\text{energy efficiency} = \frac{\text{energy output}}{\text{energy input}} \qquad (12)$$

where energy output is the sum of auroral precipitation, Joule heating and ring current. Individual storm energy

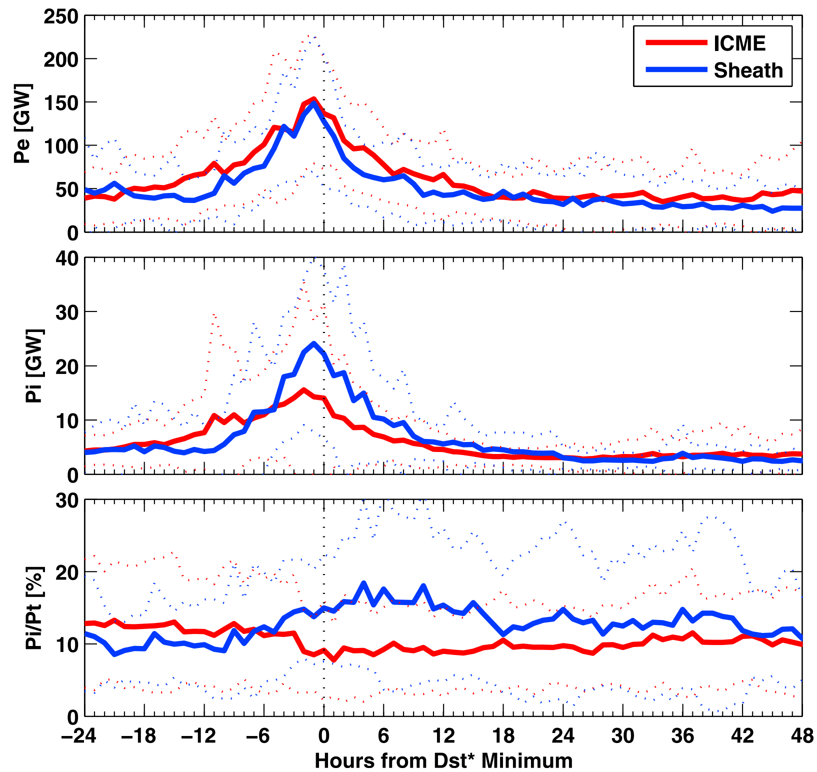

Figure 6. Superposed epoch analyses of the global auroral electron (Pe) and ion (Pi) inputs, as well as the ratio of Pi to the total (Pt = Pe + Pi) during the ICME- and sheath-driven storms. The red and blue solid lines define the mean for the ICME- and sheath-driven storms, respectively, and the dotted lines represent ±1 standard deviation.

efficiencies vary between 31% and 98% for ICMEs and between 32% and 99% for sheaths, where their mean energy efficiencies are also given in Table 1. To test the statistical significance of the means in Table 1, we calculate the Student's t statistic and its significance p [*Reiff*, 1990]. The means of both classes of events are considered to be significantly different if $p < 0.05$ [*Press et al.*, 1992]. However, the Student's t test assumes that both classes of events have the same true variance. If they have very different variances, the difference between them may be difficult to interpret [*Press et al.*, 1992]. The corresponding p values are listed in the last column of Table 1. For the ICME- and sheath-driven storms, the means of input energy ε and auroral precipitation are significantly different, whereas Joule heating, ring current and total output energy show no distinguishable differences. Electrons are dominant in auroral precipitation. The means of electron precipitation are significantly different for both classes of events. However, ion precipitation yields no distinguishable differences. The mean energy efficiency of the sheath-driven storms is 62%, while that of the ICME-driven storms is 60%, but the difference between these two classes of events is not statistically significant. The energy efficiency agrees reasonably well with the result of *Turner et al.* [2009] where the mean energy efficiency of the CME-driven storms is 62.7%.

[25] Table 2 shows the energy partitioning for the ICME- and sheath-driven storms. Ionospheric processes account for the vast majority of the energy, with the ring current only being 12%–14% of the total. It should be noted that, owing to a lack of reliable estimates, other processes cannot be provided here, such as plasmoids [see *Ieda et al.*, 1998] and plasma sheet heating. However, excluding those processes, the energy partitioning for both classes of events is similar, as both classes of events distribute the available energy to the ionosphere and ring current in comparable ratios.

5. Discussion

[26] It is interesting to test the statistical significance of the means in Figures 1–6. Typically, we calculate the Student's t statistic and its significance for each parameter at the time point of peak value between the ICME-driven storms and the sheath-driven storms. The results of the Student's t test for the peaks of various parameters are listed in Table 3.

Table 1. Mean Values of Energy Budget and Energy Efficiency for Entire Storm[a]

	ICME (10^{16} J)	Sheath (10^{16} J)	p (t test)
Energy input (ε)	18.22	12.22	0.0474
Electron precipitation	1.06	0.77	0.0006
Ion precipitation	0.11	0.12	0.4747
Auroral precipitation	1.17	0.89	0.0024
Joule heating	5.76	5.12	0.4951
Ring current	1.01	0.93	0.4004
Total output energy	7.94	6.94	0.3511
Energy efficiency (%)	60	62	0.6542

[a]The entire storm is considered to begin at the first decrease in *Dst** and end when the *Dst** has recovered 80% from its lowest value.

Table 2. Mean Values of Energy Partitioning for Entire Storm

	ICME (%)	Sheath (%)
Auroral precipitation	14.7	12.8
Joule heating	72.6	73.8
Ring current	12.7	13.4

Note that if peaks do not appear simultaneously, we do the Student's *t* test for the peak value of the sheath-driven storms and the nonpeak value of the ICME-driven storms at the same epoch time. Among all the selected parameters, the peaks of the solar wind speed v, the density N, the dynamic pressure Pdyn, the *AU* index, the *Kp* index, the *ASYH* index, the ion precipitation, the ratio of Pi/Pt and the ring current are significantly different for both classes of events. The *ASYH* peak in the sheath-driven storms results from the increase in the dynamic pressure Pdyn [*Shi et al.*, 2006]. Because the *AU* index is governed by the directly driven electric field in the dusk sector and the solar Hall conductance [*Ahn et al.*, 1999], the sheath-driven peak in *AU* signifies larger electric fields around 4 h prior to the zero epoch, which also appear in the *AL* index at the same time.

[27] Pi/Pt for the sheath-driven storms is larger than that for the ICME-driven storms within the period from −6 h to 48 h of the epoch (see Figure 6). This feature is consistent with the particle precipitation observation during a double peaked magnetic storm period (17–18 April 2002), which is illustrated in the work of *Fang et al.* [2007, Figure 9]. The first peak was driven by the sheath region preceding an ICME while the second one was due to the ICME itself. The ratio of the ion (<20 keV) to the total (electron and ion) in the northern hemisphere is about 18% during the sheath region passage, compared to 5% during the ICME passage. According to *Mende et al.* [2002], one of proton precipitation processes into the nightside from the tail is through scatting in stretched field line configurations as exist during substorm growth phase, or during the sheath region passage. So the stretched field line configuration could partly explain why there are more ions during the sheath-driven storms than during the ICME-driven storms. More recently, the simulation research of *Brambles et al.* [2010] indicated that slow dense outflows of O+ result in higher O+ densities closer to Earth, which lead to higher ring current number fluxes and the stretched magnetotail configuration. Electrons and ions both can precipitate into the night region from the tail, and the extra O+ densities should lead to more nightside precipitation. Thus, the extra O+ in the near tail could also explain why more ions precipitate during the sheath-driven storms.

[28] Our results suggest that these two classes of events are different in energy transfer as well as in geomagnetic responses. However, it is not known what physical mechanism leads to these differences. Referring back to Figures 1 and 2, we find that the Borovsky parameter does not display similar trends to that observed in the dawn-to-dusk electric field for both classes of events. For instance, the peak value of Ey is larger for the ICME-driven storms while that of the Borovsky parameter is larger for the sheath-driven storms. This indicates that although the solar wind largely controls the rate of the dayside reconnection, the solar wind control is not directly via the dawn-to-dusk electric field of the solar wind, rather there is a more complicated control that involves other solar wind parameters, such as solar wind pressure and Mach number [*Borovsky*, 2008; *Guo et al.*, 2010a]. In the previous studies, the effect of solar wind dynamic pressure on the dayside reconnection rate has been investigated by looking at dayside ionospheric convection changes, and the results suggest that the solar wind dynamic pressure strongly affects dayside reconnection as well as polar-cap convection [e.g., *Boudouridis et al.*, 2007]. Furthermore, *Palmroth et al.* [2003, 2004a, 2004b] found that the solar wind dynamic pressure has a role in ionospheric power dissipation. In this work, we observed obvious differences in solar wind pressure and Mach number in Figure 1 between these two classes of events. Therefore, we suggest that the differences in the energy transfer might be the effects of dynamic pressure and Mach number.

[29] The relative role of ionospheric Joule heating in the global magnetospheric energy budget is an important issue. When *Perreault and Akasofu* [1978] derived the epsilon parameter, it was generally believed that ~90% of energy dissipation would be through ring current injection, but this value has been gradually changing [e.g., *Knipp et al.*, 1998; *Lu et al.*, 1998; *Turner et al.*, 2001; *Tanskanen et al.*, 2002]. Recent results of *Turner et al.* [2009] show that Joule heating actually dominates over the ring current as a dissipation channel during storm events. For the storms driven by CMEs, their estimates suggest that Joule heating accounts for ~71.3% of the energy dissipation whereas the ring current accounts only for ~11.5%. For the intense storms driven by ICMEs or sheath regions, our results show that Joule heating accounts for ~73% of the energy dissipation whereas the ring current accounts only for ~13%. Moreover, the energy partitioning for these two classes of events is similar.

[30] The magnitude of the ring current energy injection rate depends strongly on the decay time. In the present

Table 3. Student's *t* Test for Peaks of Various Parameters During the ICME- and Sheath-Driven Storms[a]

	ICME	Sheath	*p* (*t* Test)
Bz (nT)	−15.1	−12.2	0.4379
v (km/s)	526	643	0.0169
Ey (mV/m)	8.3	7.13	0.7576
N (cm^{-3})	12.4	15.8	0.0027
Pdyn (nPa)	6.8	12.0	0.0025
M_A	4.9	7.2	0.1572
Newell parameter	263	290	0.8208
Borovsky parameter	4913	6038	0.2682
AL (nT)	−769	−805	0.7500
AU (nT)	251	330	0.0022
PCN	5.1	6.3	0.0590
Kp	6.6	7.4	0.0332
ASYH (nT)	120	166	0.0077
SYM-H (nT)	−155	−160	0.8135
*Dst** (nT)	−163	−176	0.5403
Epsilon (GW)	4203	4484	0.8483
Electron precipitation (GW)	153	149	0.8063
Ion precipitation (GW)	15	24	0.0234
Pi/Pt (%)	9.1	18.4	0.0030
Auroral precipitation (GW)	168	173	0.8350
Joule heating (GW)	935	1049	0.6157
Ring current (GW)	214	329	0.0490
Total output energy (GW)	1317	1551	0.2457

[a]Here *p* stands for the *t* statistic's significance; a small value (<0.05) of *p* indicates that peaks are significantly different.

study, we have used the constant τ value (8 h) as suggested by *Vichare et al.* [2005] for intense geomagnetic storms. The statistical work of *Dasso et al.* [2002] shows that the decay time spans from ~6 to 23 h, with a mean value of τ = 14 ± 4 h in the recovery phases, and τ tends to decrease as the strength of the storm increases for very intense storms (*Dst* ≤ −250 nT). To examine the influence of the different decay time on the ring current energy injection rate, we re-estimate the average ring current injection rate for each storm using different τ values. The results show that the ring current accounts for ~22%, 16%, 13%, 11%, 8.5%, and 6.5% of the energy dissipation with τ = 4, 6, 8, 10, 14, and 20 h, respectively.

6. Concluding Remarks

[31] The intense storm events driven by ICMEs and sheath regions during the period 1996–2006 are selected to examine similarities and differences in the temporal evolution of energy transfer as well as energy partitioning. The main conclusions of the present study can be summarized as follows:

[32] 1. The solar wind-magnetosphere coupling functions and geomagnetic indices show a more gradual increase and recovery during the ICME-driven storms than they do during the sheath-driven storms. However, the sheath-driven storms have larger peak values. The dawn-to-dusk electric fields do not display similar trends to those observed in the coupling functions, which suggest that the solar wind-magnetosphere coupling is not directly via the dawn-to-dusk electric field, rather there is a more complicated control that involves other solar wind parameters, such as solar wind pressure and Mach number.

[33] 2. In general, solar wind energy input (the epsilon parameter) and dissipation show similar trends as the coupling functions for both classes of events.

[34] 3. The trends of ion precipitation and the ratio of ion precipitation to the total (ion and electron) are quite different for both classes of events. There are more precipitating ions during the peak of sheath-driven storms, but less leading up to the storm at −12 h. Thus the ratio of ions to the total precipitation is significantly higher for sheath-driven storms from about 0 to +12 h.

[35] 4. For both classes of events, the means of input energy and auroral precipitation are significantly different, whereas Joule heating, ring current and total output energy show no distinguishable differences. Electrons are dominant in auroral precipitation. The means of electron precipitation are significantly different for both classes of events. In spite of significant differences around the peak of the storm, the means of ion precipitation gives us no distinguishable differences over the entire storm. The mean energy efficiency of the sheath-driven storms is 62%, while that of the ICME-driven storms is 60%, but the difference between these two classes of events is not statistically significant. Ionospheric processes account for the vast majority of the energy, with the ring current only being 12%–14% of the total. Moreover, the energy partitioning for both classes of events is similar.

[36] **Acknowledgments.** The OMNI solar wind database is compiled by the Space Physics Data Facility at the NASA Goddard Space Flight Center. The geomagnetic data are obtained through the World Data Center in Kyoto. The original DMSP and NOAA satellite auroral hemispheric power estimates were provided by the USAF Research Laboratory, Hanscom AFB, Massachusetts, and by the Space Weather Prediction Center, Boulder, Colorado, via the Coupling, Energetics and Dynamics of Atmospheric Regions database, which is supported by the National Science Foundation. Additional NOAA electron and ion hemispheric powers were supplied by David S. Evans of the Space Weather Prediction Center at NOAA. This work is jointly supported by the National Natural Science Foundation of China (40890162, 40921063, 40904049, and 41004082), the Specialized Research Fund for State Key Laboratories, and Ocean Public Welfare Scientific Research Project (201005017), State Oceanic Administration, China. Intersatellite calibration work by Barbara Emery at the National Center for Atmospheric Research is supported by the National Science Foundation.

[37] Philippa Browning thanks the reviewers for their assistance in evaluating this paper.

References

Ahn, B.-H., B. A. Emery, H. W. Kroehl, and Y. Kamide (1999), Climatological characteristics of the auroral ionosphere in terms of electric field and ionospheric conductance, *J. Geophys. Res.*, *104*, 10,031–10,040, doi:10.1029/1999JA900043.

Akasofu, S.-I. (1981), Energy coupling between the solar wind and the magnetosphere, *Space Sci. Rev.*, *28*, 121–190, doi:10.1007/BF00218810.

Baker, D. N., N. E. Turner, and T. I. Pulkkinen (2001), Energy transport and dissipation in the magnetosphere during geomagnetic storms, *J. Atmos. Sol. Terr. Phys.*, *63*, 421–429, doi:10.1016/S1364-6826(00)00169-3.

Borovsky, J. E. (2008), The rudiments of a theory of solar wind/magnetosphere coupling derived from first principles, *J. Geophys. Res.*, *113*, A08228, doi:10.1029/2007JA012646.

Boudouridis, A., L. R. Lyons, E. Zesta, and J. M. Ruohoniemi (2007), Dayside reconnection enhancement resulting from a solar wind dynamic pressure increase, *J. Geophys. Res.*, *112*, A06201, doi:10.1029/2006JA012141.

Brambles, O. J., W. Lotko, P. A. Damiano, B. Zhang, M. Wiltberger, and J. Lyon (2010), Effects of causally driven cusp O+ outflow on the storm time magnetosphere-ionosphere system using a multifluid global simulation, *J. Geophys. Res.*, *115*, A00J04, doi:10.1029/2010JA015469.

Burton, R. K., R. L. McPherron, and C. T. Russell (1975), An empirical relationship between interplanetary conditions and *Dst*, *J. Geophys. Res.*, *80*, 4204–4214, doi:10.1029/JA080i031p04204.

Dasso, S., D. Gómez, and C. H. Mandrini (2002), Ring current decay rates of magnetic storms: A statistical study from 1957 to 1998, *J. Geophys. Res.*, *107*(A5), 1059, doi:10.1029/2000JA000430.

Emery, B. A., V. Coumans, D. S. Evans, G. A. Germany, M. S. Greer, E. Holeman, K. Kadinsky-Cade, R. J. Rich, and W. Xu (2008), Seasonal, *Kp*, solar wind, and solar flux variations in long-term single-pass satellite estimates of electron and ion auroral hemispheric power, *J. Geophys. Res.*, *113*, A06311, doi:10.1029/2007JA012866.

Emery, B. A., I. G. Richardson, D. S. Evans, R. J. Rich, and W. Xu (2009), Solar wind structure sources and periodicities of global electron hemispheric power over three solar cycles, *J. Atmos. Sol. Terr. Phys.*, *71*, 1157–1175, doi:10.1016/j.jastp.2008.08.005.

Fang, X., M. W. Liemohn, J. U. Kozyra, D. S. Evans, A. D. DeJong, and B. A. Emery (2007), Global 30–240 keV proton precipitation in the 17–18 April 2002 geomagnetic storms: 1. Patterns, *J. Geophys. Res.*, *112*, A05301, doi:10.1029/2006JA011867.

Feldstein, Y. I., L. A. Dremukhina, A. E. Levitin, U. Mall, I. I. Alexeev, and V. V. Kalegaev (2003), Energetics of the magnetosphere during the magnetic storm, *J. Atmos. Sol. Terr. Phys.*, *65*, 429–446, doi:10.1016/S1364-6826(02)00339-5.

Forsyth, R. J., et al. (2006), ICMEs in the inner heliosphere: Origin, evolution and propagation effects, *Space Sci. Rev.*, *123*, 383–416, doi:10.1007/s11214-006-9022-0.

Gonzalez, W. D., and B. T. Tsurutani (1987), Criteria of interplanetary parameters causing intense magnetic storms (*Dst* < −100 nT), *Planet. Space Sci.*, *35*, 1101–1109, doi:10.1016/0032-0633(87)90015-8.

Gonzalez, W. D., J. A. Joselyn, Y. Kamide, H. W. Kroehl, G. Rostoker, B. T. Tsurutani, and V. M. Vasyliunas (1994), What is a geomagnetic storm?, *J. Geophys. Res.*, *99*, 5771–5792, doi:10.1029/93JA02867.

Gopalswamy, N. (2006), Interplanetary coronal mass ejections, *Space Sci. Rev.*, *124*, 145–168, doi:10.1007/s11214-006-9102-1.

Gopalswamy, N., S. Akiyama, S. Yashiro, G. Michalek, and R. P. Lepping (2008), Solar sources and geospace consequences of interplanetary magnetic clouds observed during solar cycle 23, *J. Atmos. Sol. Terr. Phys.*, *70*, 245–253, doi:10.1016/j.jastp.2007.08.070.

Guo, J., W. Wan, J. M. Forbes, E. Sutton, R. S. Nerem, and S. Bruinsma (2008), Interannual and latitudinal variability of the thermosphere density annual harmonics, *J. Geophys. Res.*, *113*, A08301, doi:10.1029/2008JA013056.

Guo, J., X. Feng, J. Zhang, P. Zuo, and C. Xiang (2010a), Statistical properties and geoefficiency of interplanetary coronal mass ejections and their sheaths during intense geomagnetic storms, *J. Geophys. Res.*, *115*, A09107, doi:10.1029/2009JA015140.

Guo, J., X. Feng, J. M. Forbes, J. Lei, J. Zhang, and C. Tan (2010b), On the relationship between thermosphere density and solar wind parameters during intense geomagnetic storms, *J. Geophys. Res.*, *115*, A12335, doi:10.1029/2010JA015971.

Huttunen, K. E. J., and H. E. J. Koskinen (2004), Importance of postshock streams and sheath region as drivers of intense magnetospheric storms and high-latitude activity, *Ann. Geophys.*, *22*, 1729–1738, doi:10.5194/angeo-22-1729-2004.

Huttunen, K. E. J., H. E. J. Koskinen, and R. Schwenn (2002), Variability of magnetospheric storms driven by different solar wind perturbations, *J. Geophys. Res.*, *107*(A7), 1121, doi:10.1029/2001JA900171.

Huttunen, K. E. J., H. E. J. Koskinen, A. Karinen, and K. Mursula (2006), Asymmetric development of magnetospheric storms during magnetic clouds and sheath regions, *Geophys. Res. Lett.*, *33*, L06107, doi:10.1029/2005GL024894.

Huttunen, K. E. J., S. P. Kilpua, A. Pulkkinen, A. Viljanen, and E. Tanskanen (2008), Solar wind drivers of large geomagnetically induced currents during the solar cycle 23, *Space Weather*, *6*, S10002, doi:10.1029/2007SW000374.

Ieda, A., S. Machida, T. Mukai, Y. Saito, T. Yamamoto, A. Nishida, T. Terasawa, and S. Kokubun (1998), Statistical analysis of the plasmoid evolution with Geotail observations, *J. Geophys. Res.*, *103*, 4453–4465, doi:10.1029/97JA03240.

Knipp, D. J., et al. (1998), An overview of the early November 1993 geomagnetic storm, *J. Geophys. Res.*, *103*, 26,197–26,220, doi:10.1029/98JA00762.

Knipp, D. J., W. K. Tobiska, and B. A. Emery (2004), Direct and indirect thermospheric heating sources for solar cycles 21–23, *Sol. Phys.*, *224*, 495–505, doi:10.1007/s11207-005-6393-4.

Koskinen, H. E. J., and K. E. J. Huttunen (2006), Geoeffectivity of coronal mass ejections, *Space Sci. Rev.*, *124*, 169–181, doi:10.1007/s11214-006-9103-0.

Koskinen, H. E. J., and E. Tanskanen (2002), Magnetospheric energy budget and the epsilon parameter, *J. Geophys. Res.*, *107*(A11), 1415, doi:10.1029/2002JA009283.

Lepping, R. P., D. B. Berdichevsky, C.-C. Wu, A. Szabo, T. Narock, F. Mariani, A. J. Lazarus, and A. J. Quivers (2006), A summary of WIND magnetic clouds for years 1995–2003: Model-fitted parameters, associated errors and classifications, *Ann. Geophys.*, *24*, 215–245, doi:10.5194/angeo-24-215-2006.

Lu, G. (2006), High speed streams, coronal mass ejections, and interplanetary shocks: A comparative study of geoeffectiveness, in *Recurrent Magnetic Storms: Corotating Solar Wind Streams*, *Geophys. Monogr. Ser.*, vol. 167, edited by B. T. Tsurutani et al., pp. 97–111, AGU, Washington, D. C.

Lu, G., et al. (1998), Global energy deposition during the January 1997 magnetic cloud event, *J. Geophys. Res.*, *103*, 11,685–11,694, doi:10.1029/98JA00897.

Mende, S. B., H. U. Frey, T. J. Immel, D. G. Mitchell, P. C. son-Brandt, and J.-C. Gérard (2002), Global comparison of magnetospheric ion fluxes and auroral precipitation during a substorm, *Geophys. Res. Lett.*, *29*(12), 1609, doi:10.1029/2001GL014143.

Newell, P. T., T. Sotirelis, K. Liou, C.-I. Meng, and F. J. Rich (2007), A nearly universal solar wind-magnetosphere coupling function inferred from 10 magnetospheric state variables, *J. Geophys. Res.*, *112*, A01206, doi:10.1029/2006JA012015.

O'Brien, T. P., and R. L. McPherron (2000), Forecasting the ring current index *Dst* in real time, *J. Atmos. Sol. Terr. Phys.*, *62*, 1295–1299, doi:10.1016/S1364-6826(00)00072-9.

Palmroth, M., T. I. Pulkkinen, P. Janhunen, and C.-C. Wu (2003), Stormtime energy transfer in global MHD simulation, *J. Geophys. Res.*, *108* (A1), 1048, doi:10.1029/2002JA009446.

Palmroth, M., P. Janhunen, T. I. Pulkkinen, and H. E. J. Koskinen (2004a), Ionospheric energy input as a function of solar wind parameters: Global MHD simulation results, *Ann. Geophys.*, *22*, 549–566, doi:10.5194/angeo-22-549-2004.

Palmroth, M., T. I. Pulkkinen, P. Janhunen, D. J. McComas, C. W. Smith, and H. E. J. Koskinen (2004b), Role of solar wind dynamic pressure in driving ionospheric Joule heating, *J. Geophys. Res.*, *109*, A11302, doi:10.1029/2004JA010529.

Perreault, P., and S.-I. Akasofu (1978), A study of geomagnetic storms, *Geophys. J. R. Astron. Soc.*, *54*, 547–573.

Press, W. H., S. A. Teukolsky, W. T. Vetterling, and B. P. Flannery (1992), *Numerical Recipes: The Art of Scientific Computing*, 2nd ed., Cambridge Univ. Press, New York.

Pulkkinen, T. I., N. Y. Ganushkina, E. I. Kallio, G. Lu, D. N. Baker, N. E. Turner, T. A. Fritz, J. F. Fennell, and J. Raeder (2002), Energy dissipation during a geomagnetic storm: May 1998, *Adv. Space Res.*, *30*, 2231–2240, doi:10.1016/S0273-1177(02)80232-0.

Pulkkinen, T. I., N. Partamies, K. E. J. Huttunen, G. D. Reeves, and H. E. J. Koskinen (2007), Differences in geomagnetic storms driven by magnetic clouds and ICME sheath regions, *Geophys. Res. Lett.*, *34*, L02105, doi:10.1029/2006GL027775.

Reiff, P. H. (1990), The use and misuse of statistics in space physics, *J. Geomagn. Geoelectr.*, *42*, 1145–1174.

Richardson, I. G., H. V. Cane, and E. W. Cliver (2002), Sources of geomagnetic activity during nearly three solar cycles (1972–2000), *J. Geophys. Res.*, *107*(A8), 1187, doi:10.1029/2001JA000504.

Shi, Y., E. Zesta, L. R. Lyons, K. Yumoto, and K. Kitamura (2006), Statistical study of effect of solar wind dynamic pressure enhancements on dawn-to-dusk ring current asymmetry, *J. Geophys. Res.*, *111*, A10216, doi:10.1029/2005JA011532.

Tanskanen, E., T. I. Pulkkinen, H. E. J. Koskinen, and J. A. Slavin (2002), Substorm energy budget during low and high solar activity: 1997 and 1999 compared, *J. Geophys. Res.*, *107*(A6), 1086, doi:10.1029/2001JA900153.

Thomsen, M. F. (2004), Why *Kp* is such a good measure of magnetospheric convection, *Space Weather*, *2*, S11004, doi:10.1029/2004SW000089.

Tsurutani, B. T., W. D. Gonzalez, F. Tang, S. I. Akasofu, and E. J. Smith (1988), Origin of interplanetary southward magnetic fields responsible for major magnetic storms near solar maximum (1978–1979), *J. Geophys. Res.*, *93*, 8519–8531, doi:10.1029/JA093iA08p08519.

Turner, N. E., D. N. Baker, T. I. Pulkkinen, J. L. Raeder, J. F. Fennell, and V. K. Jordanova (2001), Energy content in the stormtime ring current, *J. Geophys. Res.*, *106*, 19,149–19,156, doi:10.1029/2000JA003025.

Turner, N. E., E. J. Mitchell, D. J. Knipp, and B. A. Emery (2006), Energetics of magnetic storms driven by corotating interaction regions: A study of geoeffectiveness, in *Recurrent Magnetic Storms: Corotating Solar Wind Streams*, *Geophys. Monogr. Ser.*, vol. 167, edited by B. T. Tsurutani et al., pp. 113–124, AGU, Washington, D. C.

Turner, N. E., W. D. Cramer, S. K. Earles, and B. A. Emery (2009), Geoefficiency and energy partitioning in CIR-driven and CME-driven storms, *J. Atmos. Sol. Terr. Phys.*, *71*, 1023–1031, doi:10.1016/j.jastp.2009.02.005.

Vichare, G., S. Alex, and G. S. Lakhina (2005), Some characteristics of intense geomagnetic storms and their energy budget, *J. Geophys. Res.*, *110*, A03204, doi:10.1029/2004JA010418.

Yermolaev, Y. I., M. Y. Yermolaev, N. S. Nikolaeva, and I. G. Lodkina (2007), Interplanetary conditions for CIR-induced and MC-induced geomagnetic storms, *Bulg. J. Phys.*, *34*, 128–135.

Yermolaev, Y. I., N. S. Nikolaeva, I. G. Lodkina, and M. Y. Yermolaev (2009), Catalog of large-scale phenomena of solar wind during 1976–2000, *Cosmic Res., Engl. Transl.*, *47*, 81–94, doi:10.1134/S0010952509020014.

Zhang, J., et al. (2007), Solar and interplanetary sources of major geomagnetic storms ($Dst \leq -100$ nT) during 1996–2005, *J. Geophys. Res.*, *112*, A10102, doi:10.1029/2007JA012321.

Zhang, J., W. Poomvises, and I. G. Richardson (2008a), Sizes and relative geoeffectiveness of interplanetary coronal mass ejections and the preceding shock sheaths during intense storms in 1996–2005, *Geophys. Res. Lett.*, *35*, L02109, doi:10.1029/2007GL032045.

Zhang, J., I. G. Richardson, and D. F. Webb (2008b), Interplanetary origin of multiple-dip geomagnetic storms, *J. Geophys. Res.*, *113*, A00A12, doi:10.1029/2008JA013228.

B. A. Emery, High Altitude Observatory, NCAR, 3080 Center Green, Boulder, CO 80301, USA. (emery@ucar.edu)

X. Feng, J. Guo, F. Shen, W. Song, and C. Xiang, SIGMA Weather Group, State Key Laboratory of Space Weather, CSSAR, Chinese Academy of Sciences, Beijing 100190, China. (fengx@spaceweather.ac.cn; jpguo@spaceweather.ac.cn; fshen@spaceweather.ac.cn; wbsong@spaceweather.ac.cn; cqxiang@spaceweather.ac.cn)

J. Zhang, Department of Computational and Data Sciences, George Mason University, 4400 University Dr., MSN 6A2, Fairfax, VA 22030, USA. (jzhang7@gmu.edu)